Electronic Supplementary Material (ESI) for ChemComm.
This journal is © The Royal Society of Chemistry 2021

Self-sorting of porous $Cu_4L_2L'_2$ metal-organic cages composed of isomerisable ligands

Adrian W. Markwell-Heys, [a] Matthew L. Schneider[a] , [a] Jenica Marie L. Madridejos, [a] Gregory F. Metha [a] and Witold M. Bloch*[a]

[a]Department of Chemistry, The University of Adelaide, Adelaide, Australia.

Email: witold.bloch@adelaide.edu.au

Table of contents

1. Experimental section 3
1.2. Materials and measurements 3
1.3. Synthesis of Cu_4L_4 Cages 3
1.3.1. Preparation of DCLs 3
1.3.2. ^{1}H NMR studies of in-situ ligand synthesis and DCL formation 3
1.3.3. Synthesis of macrocycle **2** 5
1.3.4. Transformation of macrocycle **2** to **1b** or **1c** 6
2. Infrared Spectroscopy 7
3. Powder X-ray diffraction 9
4. Thermogravimetric analysis 12
5. Gas adsorption 13
6. Calculations 15
7. X-ray crystallography 17
7.1. General methods 17
7.2. Thermal ellipsoid plots 19
8. A discussion on **1b** and **1b-py** 21
9. References 23

1. Experimental section

1.2. Materials and measurements

Infrared spectra were collected on a Perkin-Elmer Spectrum 100 using a UATR sampling accessory. Thermal gravimetric analysis (TGA) was measured on a TA Instruments Discovery TGA under a constant flow of N_2 at a temperature increase rate of 10 °C/min. Powder X-ray diffraction data were collected on a Bruker Advance D8 diffractometer (capillary stage) using Cu Kα radiation (λ = 1.5418 Å, 50 kW/40mA). 1.0 mm capillaries were filled with the respective solvent before loading crystals of the samples. This was done to avoid any possible desolvation of the crystalline sample. Rietveld refinements were performed on TOPAS 4.2. Gas sorption isotherm measurements were performed on a Micromeritics 3Flex Surface Characterisation Analyser. UHP grade (99.999 %) N_2 was used for all measurements. Temperatures were maintained at 77 K or 195 K using a cryo-cooler. The isotherms were then analysed to determine the Brunauer Emmett-Teller (BET) surface area and pore-size distribution using the MicroActive software (Version 3.00, Micromeritics Instrument Corp. 2013).

1.3. Synthesis of Cu_4L_4 Cages

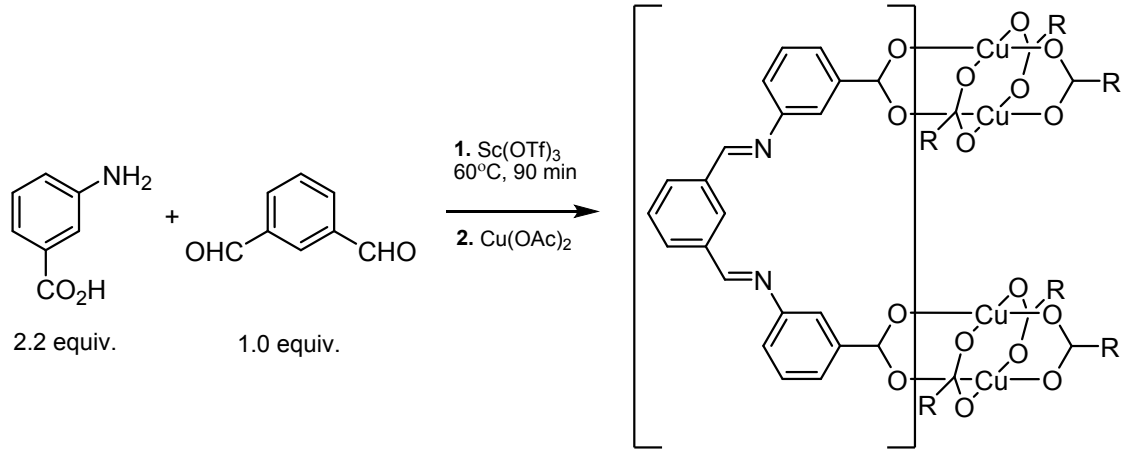

Scheme 1

1.3.1. Preparation of DCLs

m-aminobenzoic acid (45 mg, 0.328 mmol) and isophthaldialdehyde (20 mg, 0.149 mmol) and $Sc(OTf)_3$ (1.25 mg, 0.00254 mmol) were combined in either DMF (14 mL) or DMA (8 mL) and the resulting solution was heated at 60˚C for 90 minutes. Once the reaction mixture had cooled to room temperature, $Cu(OAc)_2{\cdot}H_2O$ (36 mg, 0.180 mmol) was added to the reaction vessel in one portion and sonicated until complete dissolution was observed.

1.3.2. ^{1}H NMR studies of in-situ ligand synthesis and DCL formation

^{1}H NMR experiments were carried out in DMF-d_7 to; 1) observe whether $Cu(OAc)_2$ could direct/accelerate the formation of the *in situ* generated diimine ligand (**L**), and 2) observe the dynamic combinatorial library of the Cu-imine cage system in solution. Isophathaldehyde (2.0 mg, 0.0149 mmol) and *m*-amino benzoic acid (4.5 mg, 0.0328 mmol) in DMF-d_7 (0.7 ml) served as a starting point (Fig. S1 & S2, 1). Two experiments were performed under the aforenoted conditions above, possessing the starting material precursors, one with $Sc(OTf)_3$ (Figure S1) and the other containing $Cu(OAc)_2$ (Figure S2). The progress of the imine condensation was monitored following addition of $Sc(OTf)_3$ (1 drop of 5 mg in 1 ml of DMF) at room temperature (Figure S1, **2**), then heating 60 ˚C for an extended period of time (Figure S1, **3** & **4**). The ^{1}H NMR spectrum of the reaction mixture revealed the reaction reached equilibrium after 10 minutes at room temperature (Figure S1, **2**) with the diimine ligand as the major product and mono-imine adduct as the minor product (ratio: 4:1, respectively). The reaction could not be further pushed to form more of the diimine product despite the further addition of $Sc(OTf)_3$ and heating the sample at 60 ˚C for an extended period of time (Figure S1, **4**). Following the addition of $Cu(OAc)_2$, the NMR spectrum obtained was dramatically broadened in the aromatic region (Figure S1, **5**). Due to the drastically broadened nature of the CH peaks, we assert

that this effect is not just a consequence of paramagnetic spin interference from the copper paddlewheel centre,[1,2] but also indicative of a dynamic combinatorial library in solution.[3]

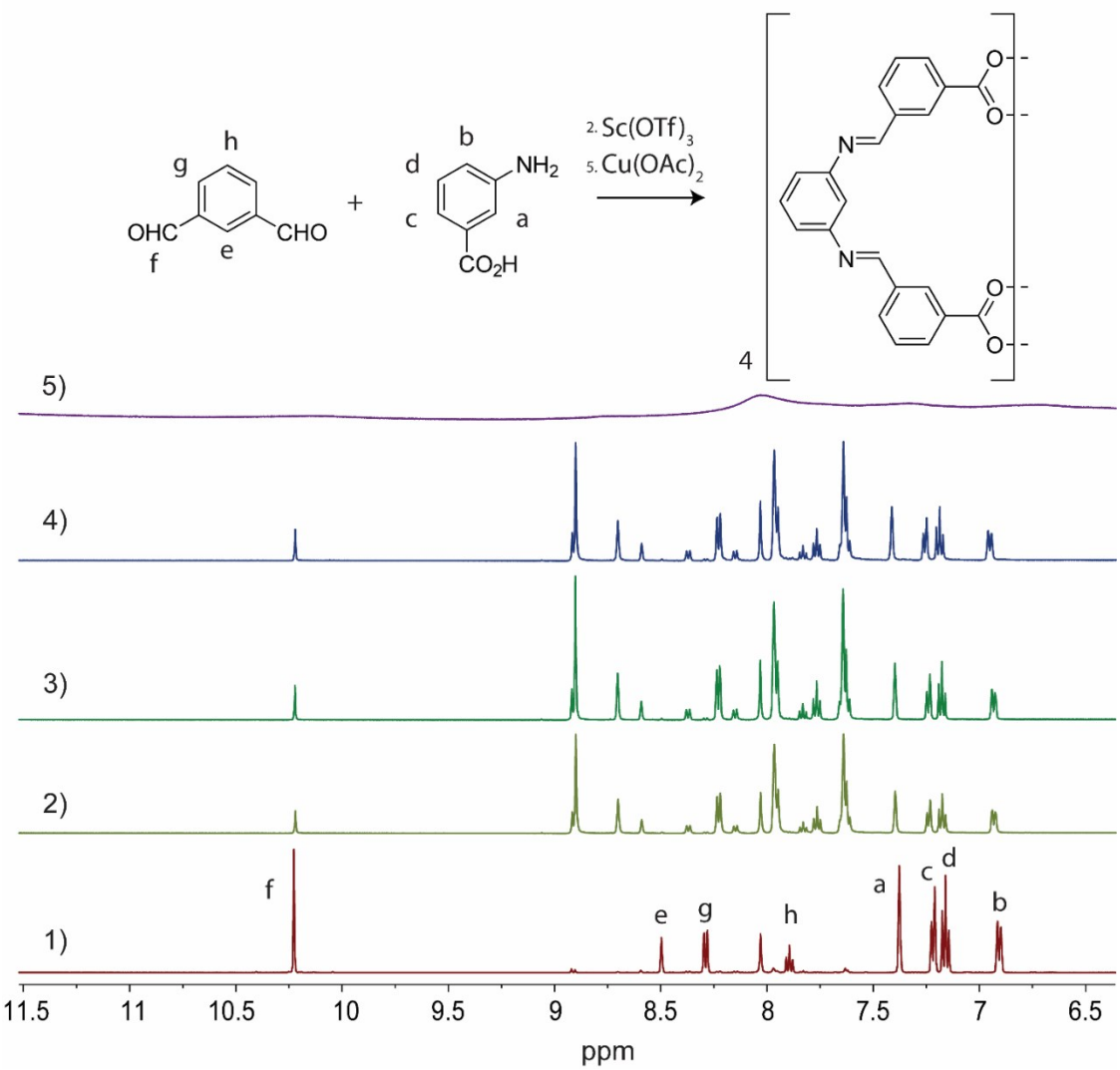

Figure S1. ^{1}H NMR experiment (500 MHz/DMF-d_7) monitoring the formation of diimine ligand from isophathaldehyde and *m*-amino benzoic acid (4.5 mg, 0.0328 mmol). **1)** starting materials Isophathaldehyde (2.0 mg, 0.0149 mmol) and *m*-amino benzoic acid **2)** addition of $Sc(OTf)_3$ (1 drop of 5 mg in 1 ml of DMF) at room temperature for *10 minutes*. Heating sample, following addition of $Sc(OTf)_3$, at 60 ˚C for **3)** *1 hour* and **4)** *48 hours*. **5)** Addition of $Cu(OAc)_2$ (3.6 mg, 0.018 mmol) at room temperature for *5 minutes*.

Comparatively, the addition of $Cu(OAc)_2$ prior to the addition of $Sc(OTf)_3$ led to significant broadening of the *m*-amino benzoic acid CH spectral peaks, but not that of isophathaldehyde (Fig. S2, **2**), indicative of coordination by the carboxylate of the former. Heating a sample of the starting precursors with $Cu(OAc)_2$ at 60 ˚C did not appear to drive the condensation of the components (Figure S2, **2**). Upon the addition of $Sc(OTf)_3$ at room temperature, a significantly broadened ^{1}H NMR spectrum was obtained (Figure S2, **3**), suggesting the formation of a DCL. Therefore, $Cu(OAc)_2$ alone does not appear to drive the condensation of the components (and thus cage formation) in the absence of the $Sc(OTf)_3$ catalyst. We note that ^{1}H NMR spectra of Cu_4L_4 cages typically show broadening only of resonances immediately adjacent to the Cu(II) paddlewheel.[2,4] Thus, the significant broadness of all resonances (particularly in Fig S1. 5) is unlikely to be due to Cu(II) coordination alone.

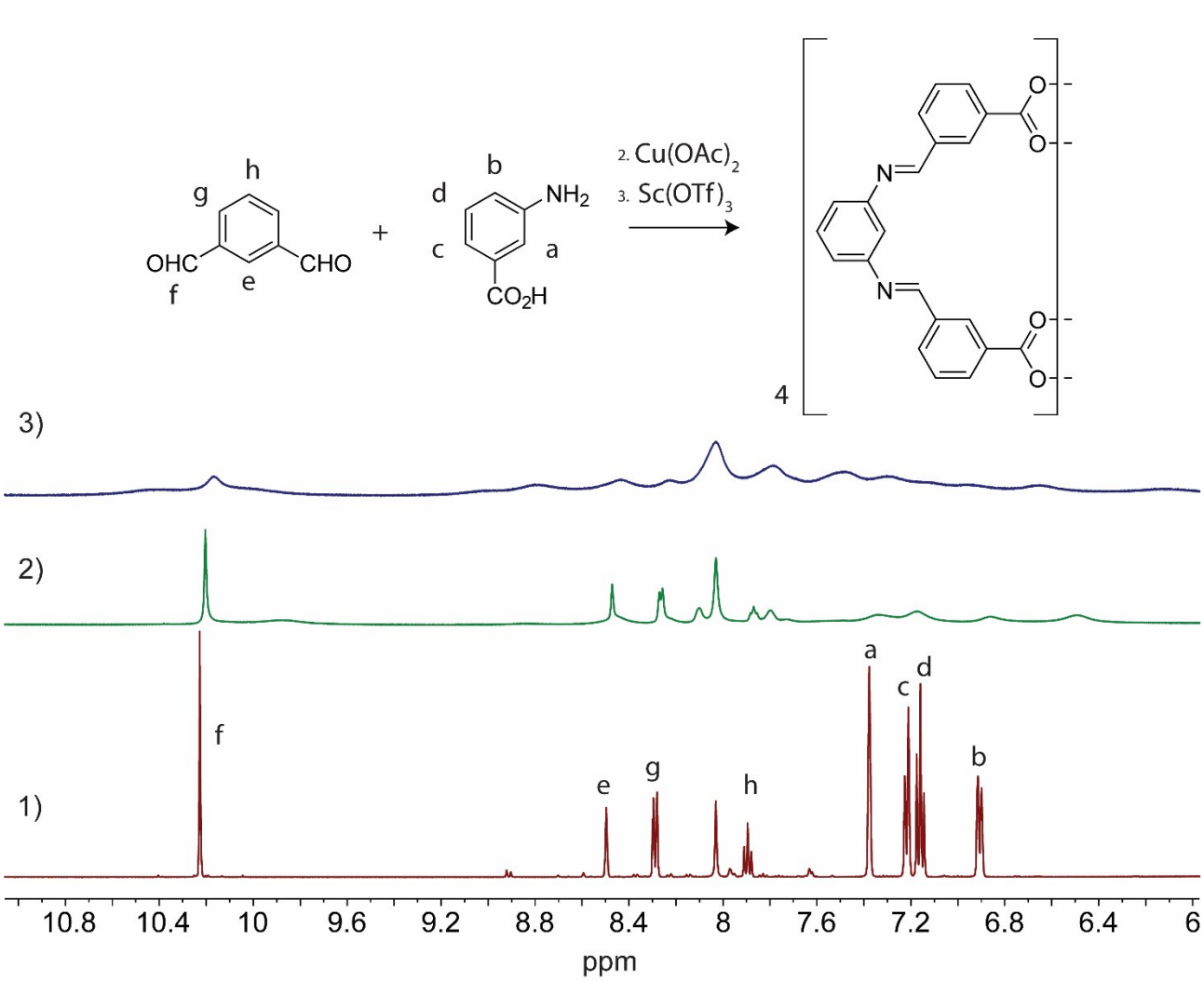

Figure S2. ^{1}H NMR spectra (500 MHz/DMF-d_7) monitoring the influence of $Cu(OAc)_2$ on the potential formation of diimine ligand in the absence of $Sc(OTf)_3$. **1)** starting materials Isophathaldehyde (2.0 mg, 0.0149 mmol) and *m*-amino benzoic acid **2)** addition of $Cu(OAc)_2$ (3.6 mg, 0.018 mmol) after heating at 60 ˚C for *1 hour*, followed by addition of **3)** $Sc(OTf)_3$ (1 drop of 5 mg in 1 ml of DMF) at room temperature for *5 minutes*.

Table S1: Crystallisation condition employed to obtain phases **1a-c**

Solvents *x/y*; slow-vapour diffusion of *y* into *x*	Crystallised phase
DMA/MeOH	**1a**
DMA/DiPE	**1b**
DMF/DiPE	**1c**

*DiPE = diisopropyl ether.

Note: the cage solids could be digested in order to verify complete formation of the diimine ligand (Fig. S3, cage disassembly, without imine hydrolysis). Digestion stock solution: to a solution of DMSO-d_6 (800 µL) and TBAOH in MeOH (1M, 800 µL), egtazic acid (EGTA, 200 mg, 0.52 mmol) was added in one portion. The solution was heated at 60 °C for 2 h until the solid dissolved.

*1.3.3. Synthesis of macrocycle **2***

A dried sample of the cage (**1a**, 80 mg) was dissolved in pyridine (0.4 mL) and an aliquot of DMF (1.4 mL) was rapidly added in one portion. The resulting solution was allowed to stand at room temperature for 48 hrs. This afforded macrocycle **2** as blue crystals.

*1.3.4. Transformation of macrocycle **2** to **1b** or **1c***

Macrocycle **2** (~30 mg) was suspended in DMA (2 mL) and was heated at 60 ˚C for 2 hrs to afford imine cage **1b** as green crystals. Similarly, performing the same reaction on DMF produce green crystals of **1c**.

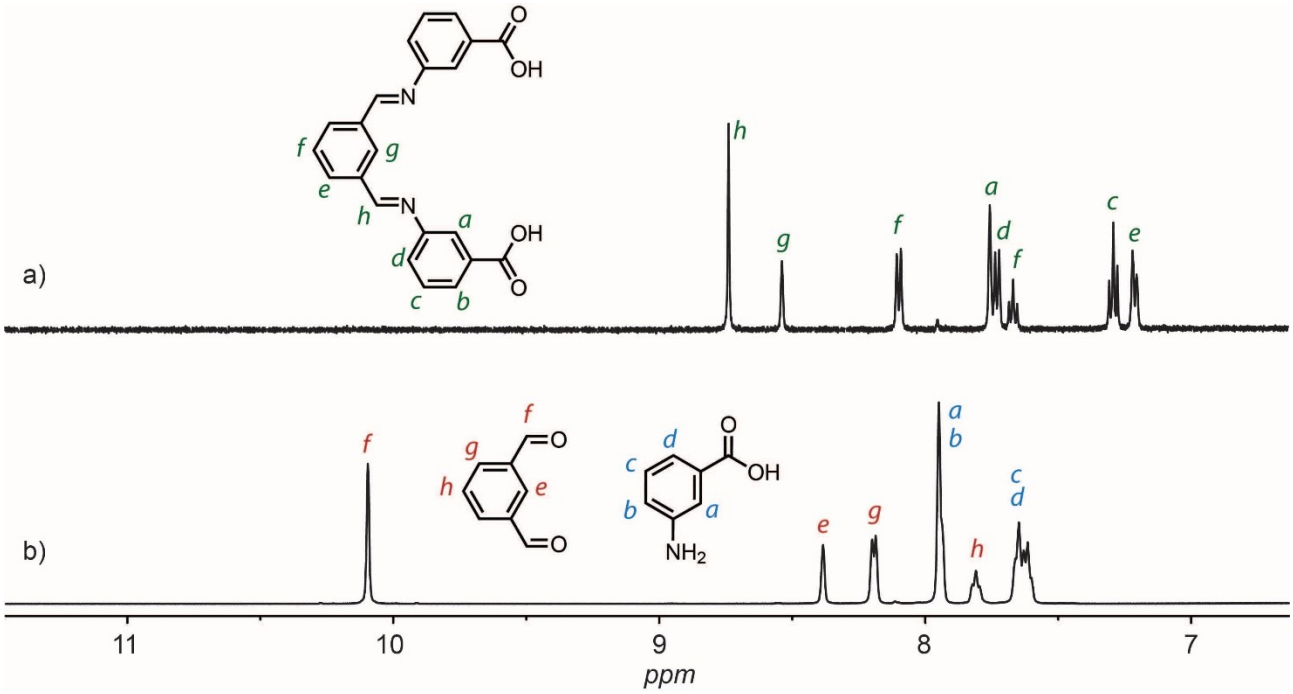

Figure S3. ^{1}H NMR spectra (500 MHz/DMSO-d_6) of two digestion methods employed to further characterise the lantern cage solids. a) digestion of **1a** (~ 2 mg) with 25 µL of EGTA digestion solution and 625 µL of DMSO-d_6; b) **1a**, digested using the conventional method (20 µL DCL, 640 µL DMSO-d_6), which clearly results in imine hydrolysis into the Isophathaldehyde and *m*-amino benzoic acid components (1:2 ratio).

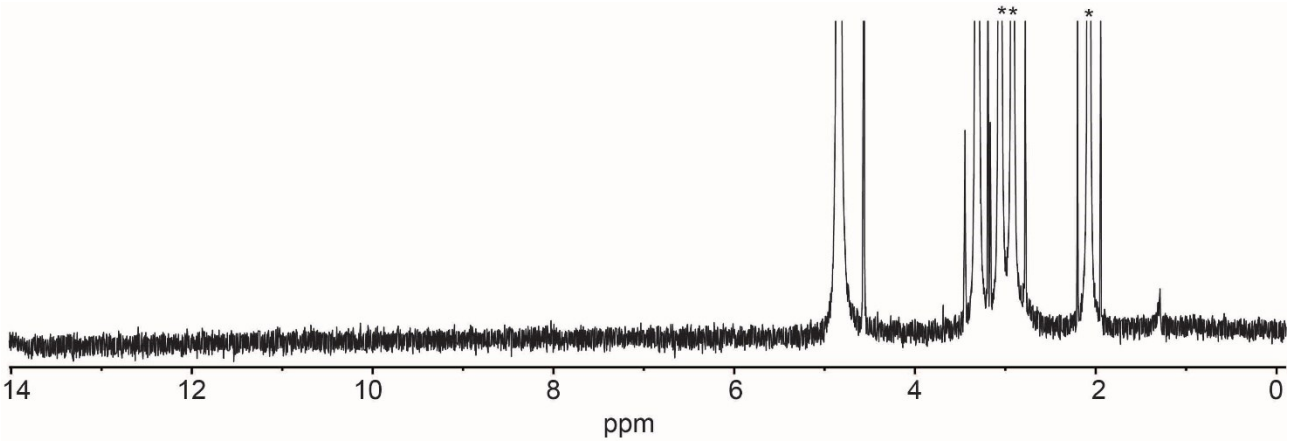

Figure S4. ^{1}H NMR spectrum (500 MHz, CD_3OD, 64 scans) of the MeOD suspension of **1b** (~5 mg in 650µL of MeOD. * = DMA. An identical spectrum could be obtained for **1a** and **1c**.

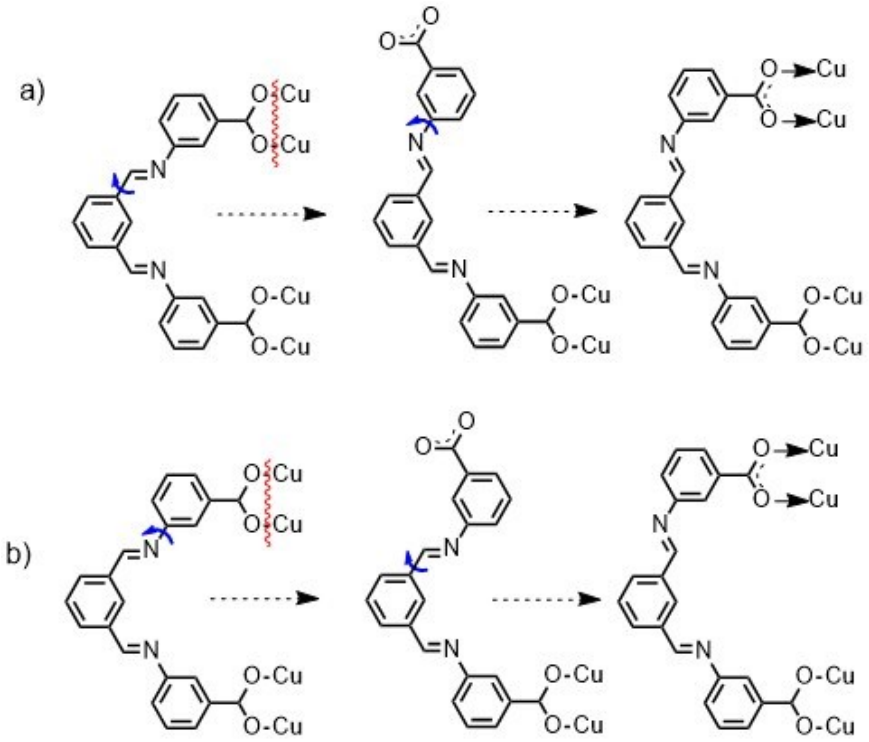

Figure S5. A scheme showing the two possible pathways for isomerising $\mathbf{L^{AA}}$ to $\mathbf{L^{SA}}$ (a & b). We assume that within the DCL, the isomerisation between $\mathbf{L^{AA}}$, $\mathbf{L^{SA}}$ and $\mathbf{L^{SS}}$ occurs concurrent with cage disassembly and reassembly. In the solid-state and during the MeOH exchanges cycles, however, it is reasonable to assume that the rotational isomerisation of the ligand is locked, due to the strong π-stacking within these solids and their insolubility in MeOH (Fig. S4). Note: ligand isomerisation (e.g L^{AA} to L^{SA}) within the crystalline cage solid would require a bond breaking event, two concomitant bond rotations followed by bond reformation.

2. Infrared Spectroscopy

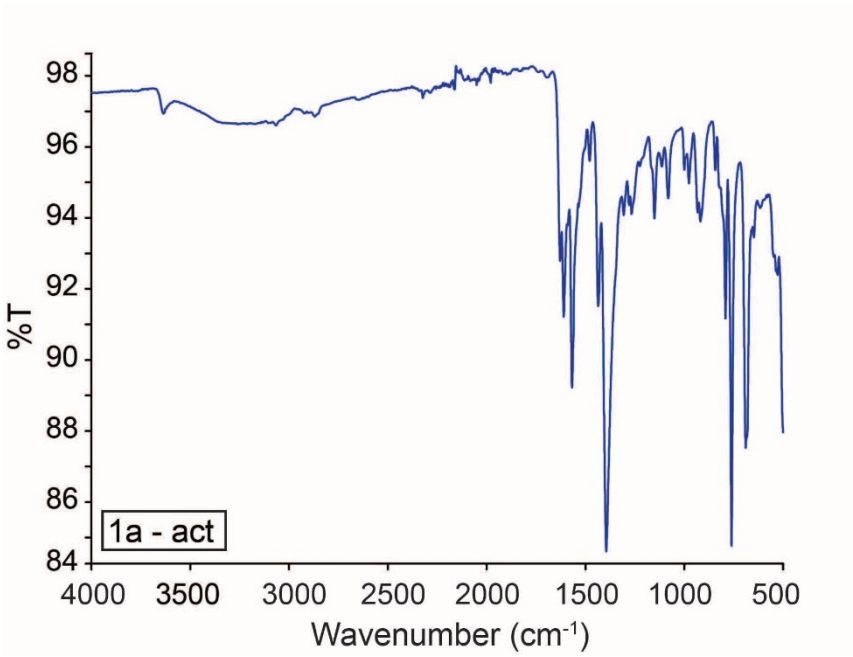

Figure S6. IR spectrum of **1a** (activated sample).

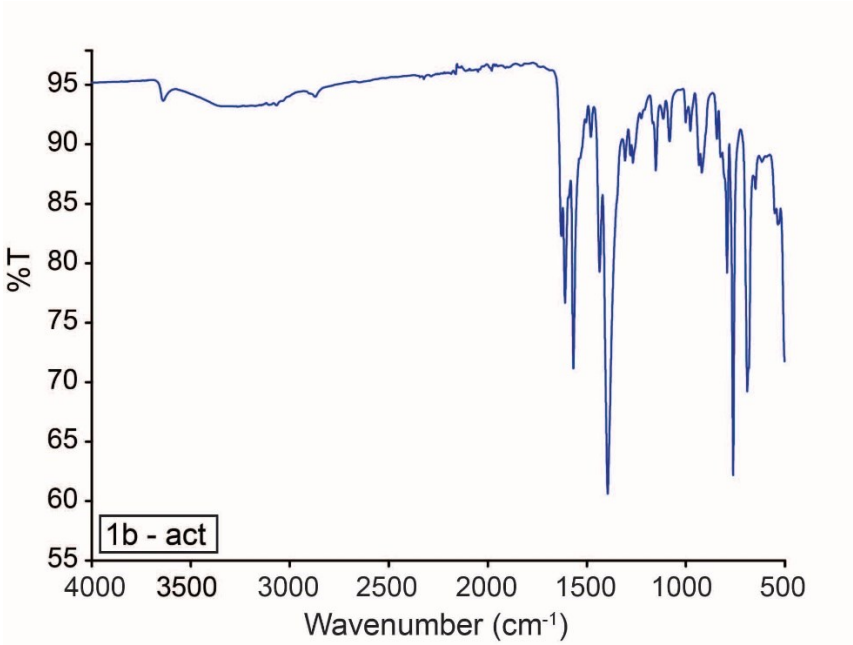

Figure S7. IR spectrum of **1b** (activated sample).

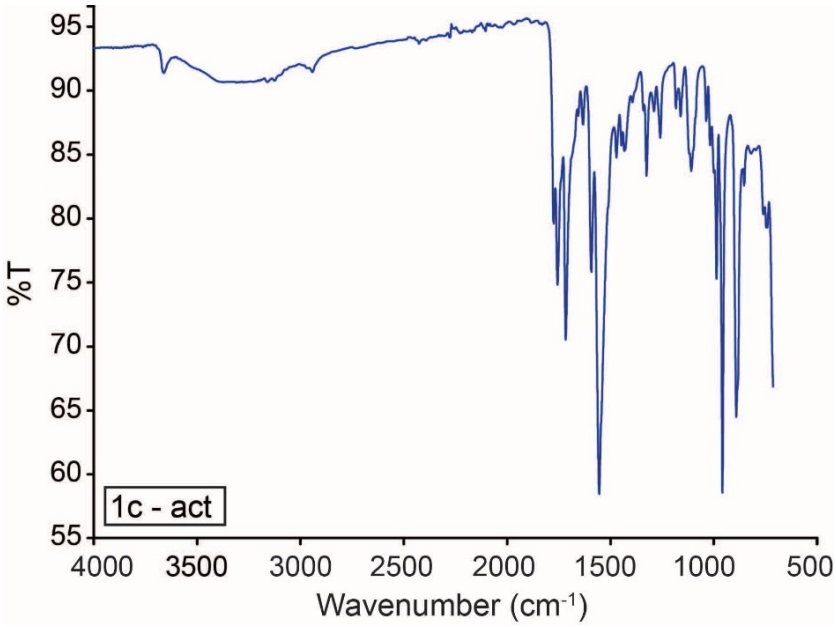

Figure S8. IR spectrum of **1c** (activated sample).

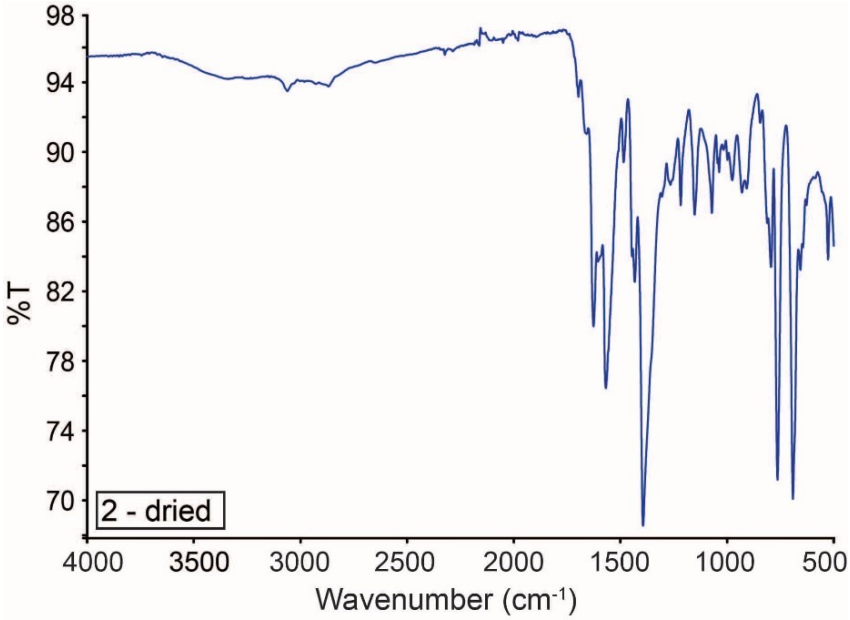

Figure S9. IR spectrum of **2** (washed with methanol and dried under high vacuum).

3. Powder X-ray diffraction

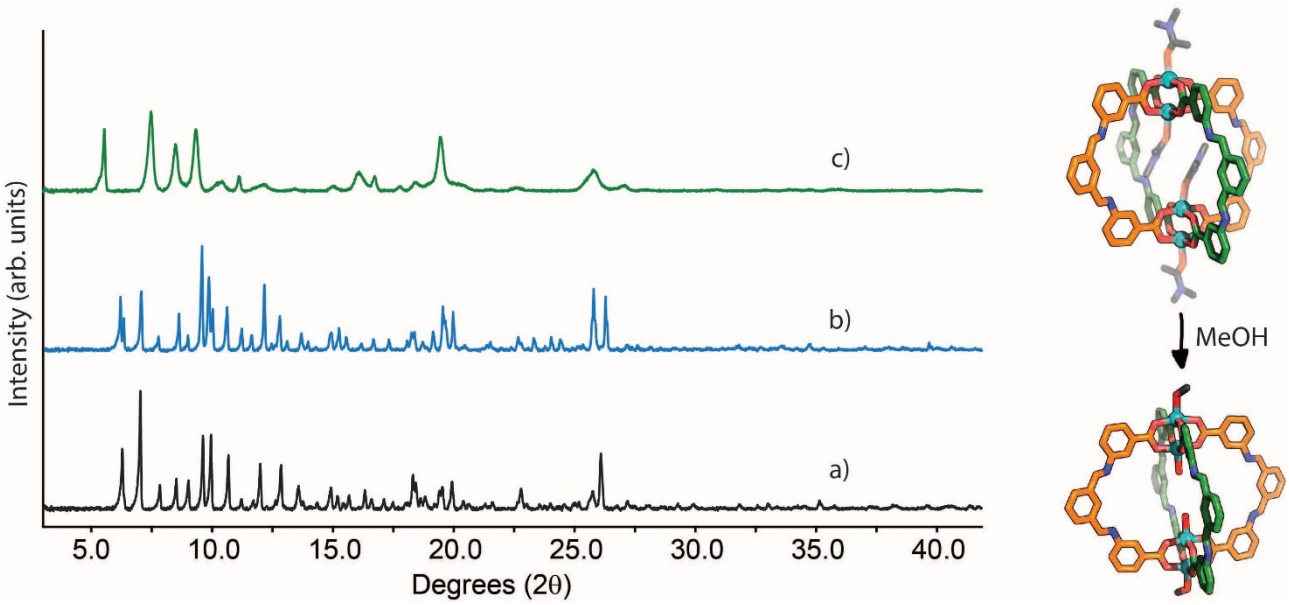

Figure S10. Left: powder X-ray diffraction patterns of **1a** showing solvent washing and activation: a) **1a** as-synthesised (DMA/MeOH); b) **1a** solvent exchanged with MeOH; c) **1a** activated sample. Right: X-ray crystal structures of **1a** and **1a-MeOH**, showing solvent exchange at the paddlewheel site and retention of ligand conformation and configuration.

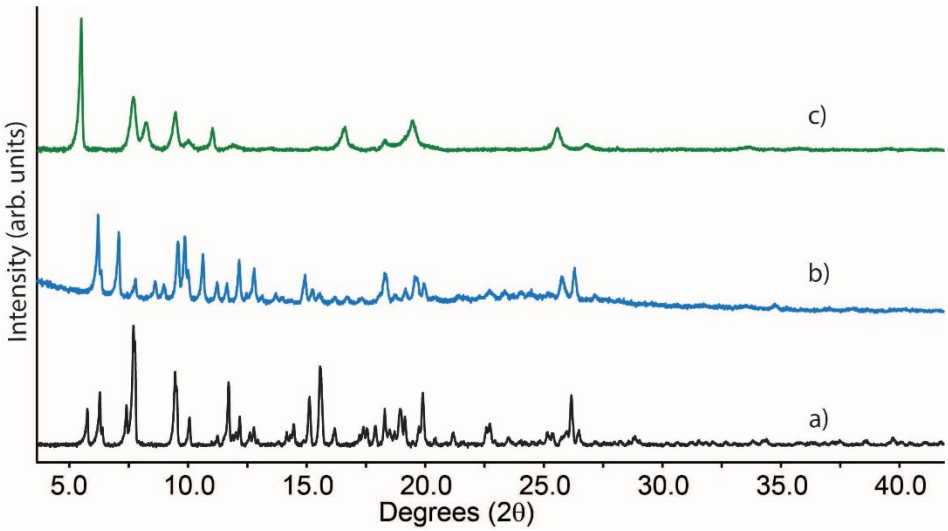

Figure S11. Powder X-ray diffraction patterns of **1b** showing solvent washing and activation: a) **1b** as-synthesised (DMA/DiPE); b) **1b** solvent exchanged with MeOH; c) **1b** activated sample.

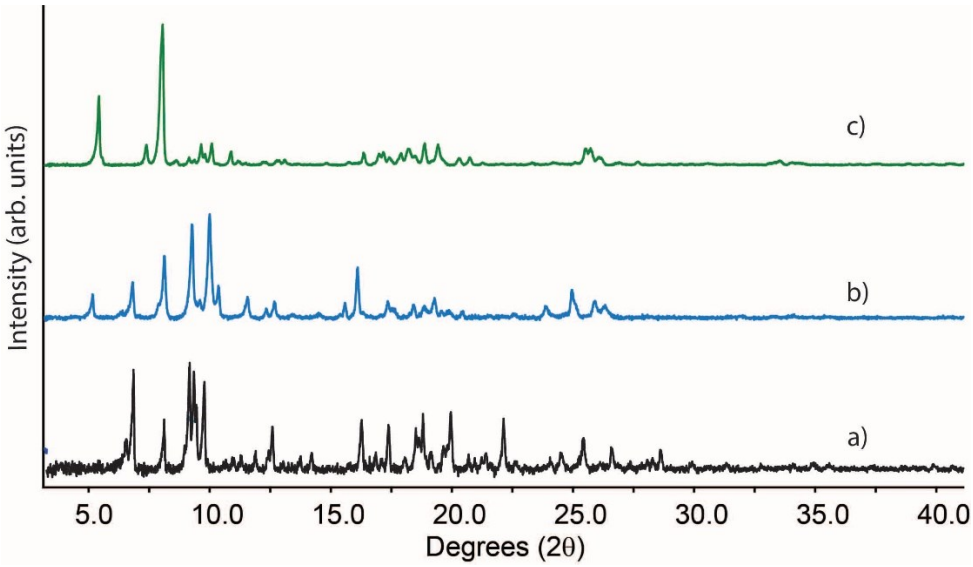

Figure S12. Powder X-ray diffraction patterns of **1c** showing solvent washing and activation: a) **1c** as-synthesised (DMF/DiPE); b) **1c** solvent exchanged with MeOH; c) **1c** activated sample.

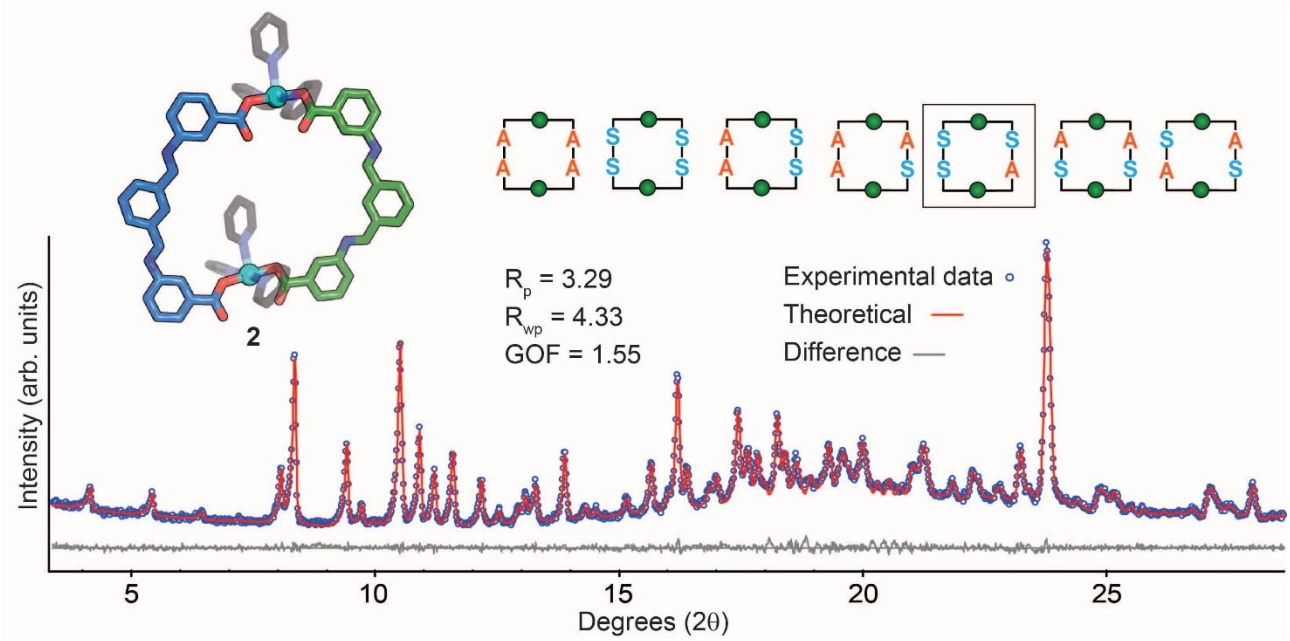

Figure S13. X-ray structure of macrocycle **2**; with the possible isomers of **2**. The observed isomer $[Cu_2L^{SA}{}_2L^{SS}{}_2(C_5H_5N)_6]$ is highlighted (**2**). Rietveld PXRD refinement of the bulk sample of **2**. The excellent fit to the experimental data indicates that the transformation to obtain the single isomer (from a possible 7) proceeds in a high fidelity.

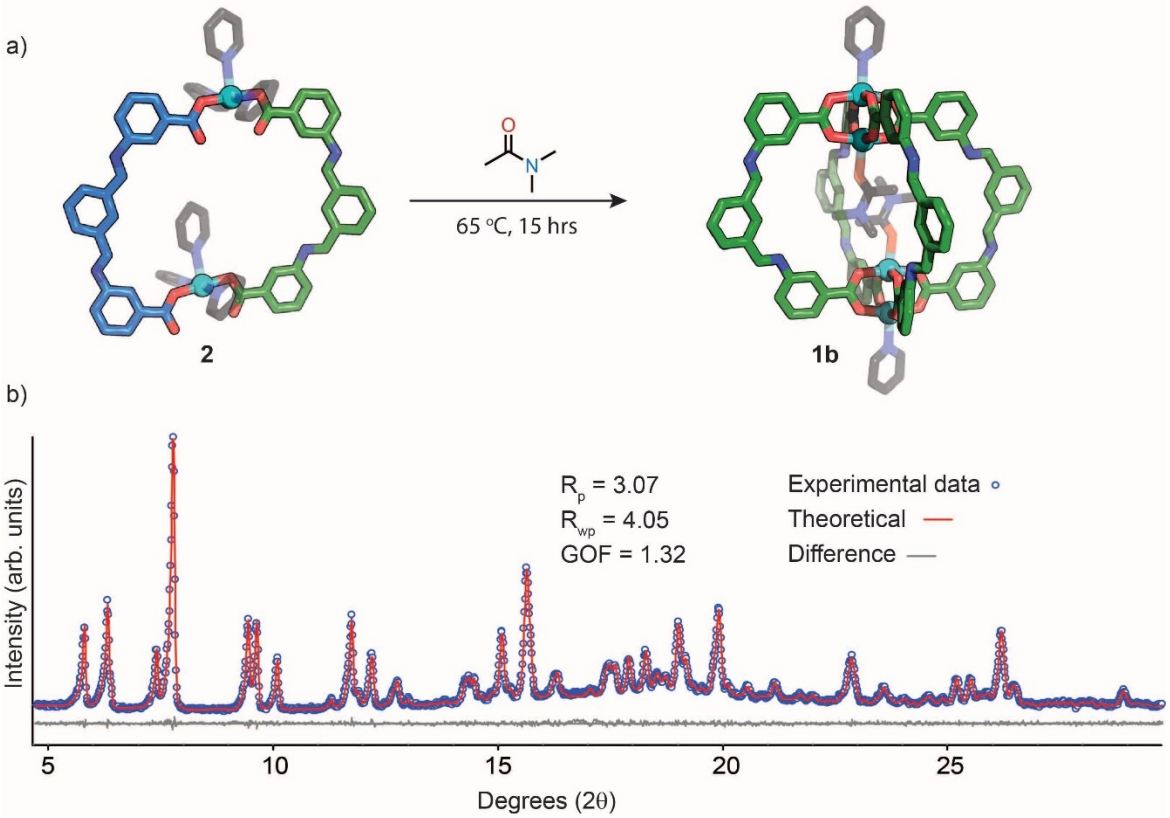

Figure S14. a) A scheme showing the transformation of macrocycle **2** to cage isomer **1b-py**, upon heating crystals of **2** in DMA (transformation occurs via recrystallisaiton). The structures shown in the scheme are X-ray structures; b) Rietveld PXRD refinement of the bulk sample of the reaction shown in a) with the single-crystal X-ray data of **1b** measured from the same sample $(Cu_4L^{SA}{}_4(C_5H_5N)_2(DMA)_2]$. The excellent agreement indicates that the transformation to obtain a single isomer proceeds in a high fidelity.

4. Thermogravimetric analysis

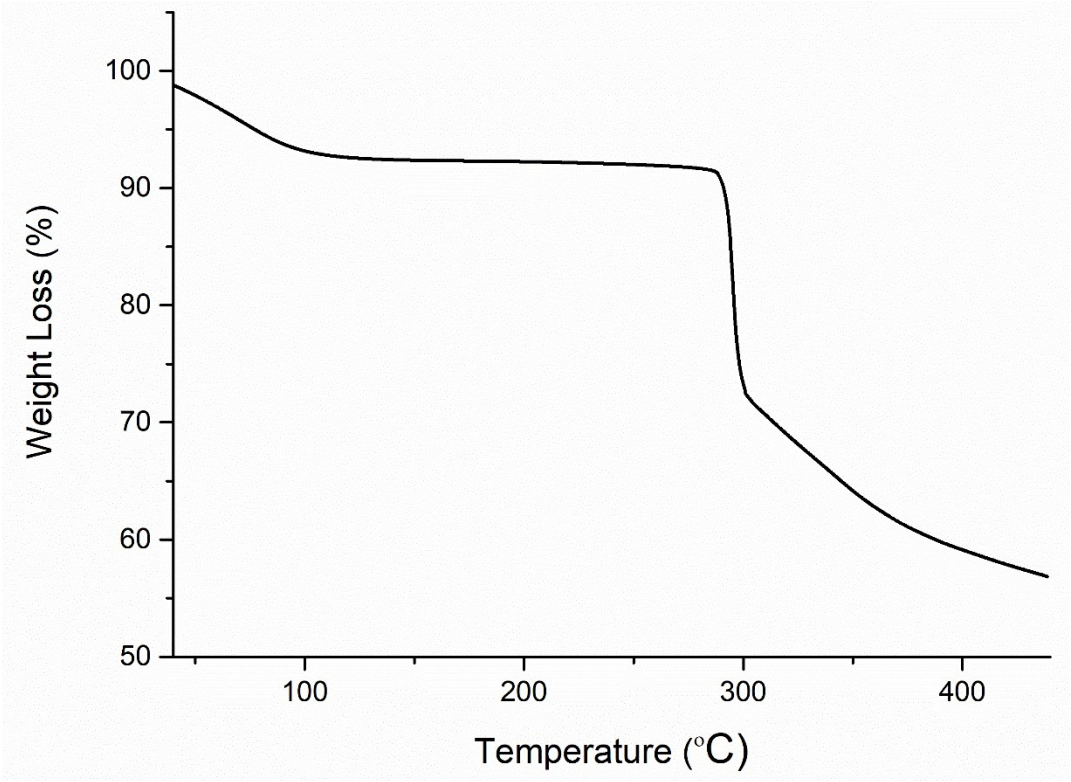

Figure S15. TGA trace of **1a.** A solvent weight loss of 7% is apparent between 30 – 130 °C with decomposition occurring at ~295 °C

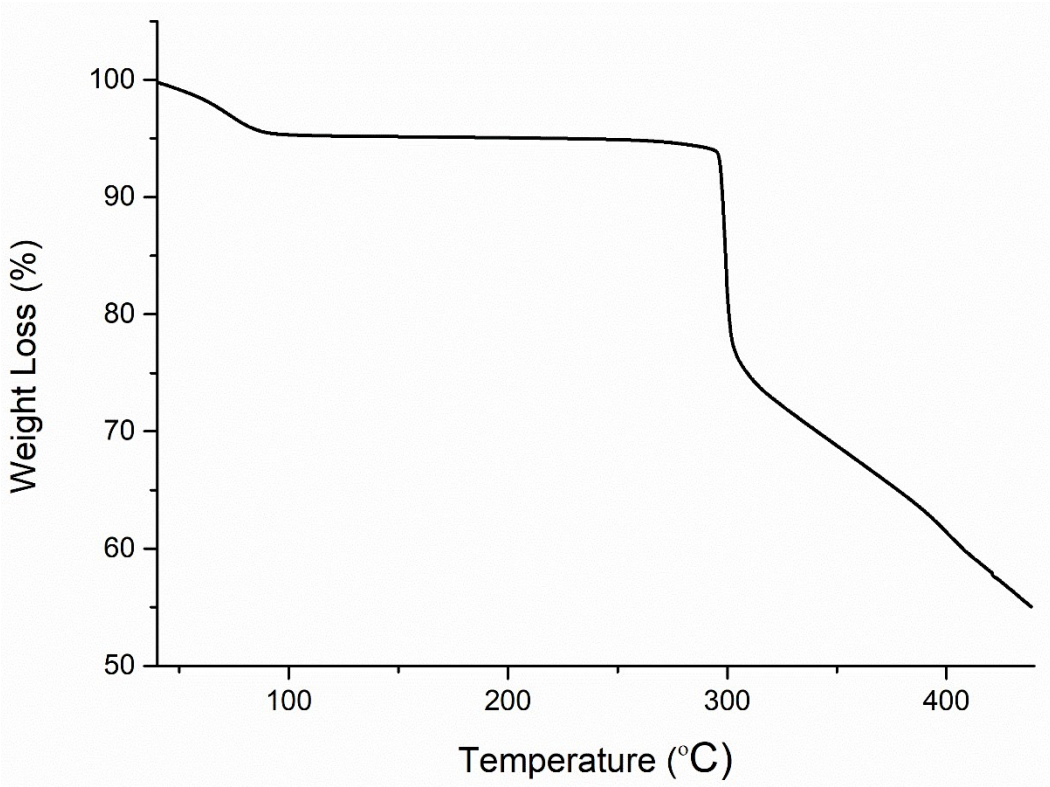

Figure S16. TGA trace of **1b.** A solvent weight loss of 5% is apparent between 30 – 100 °C with decomposition occurring at ~295 °C

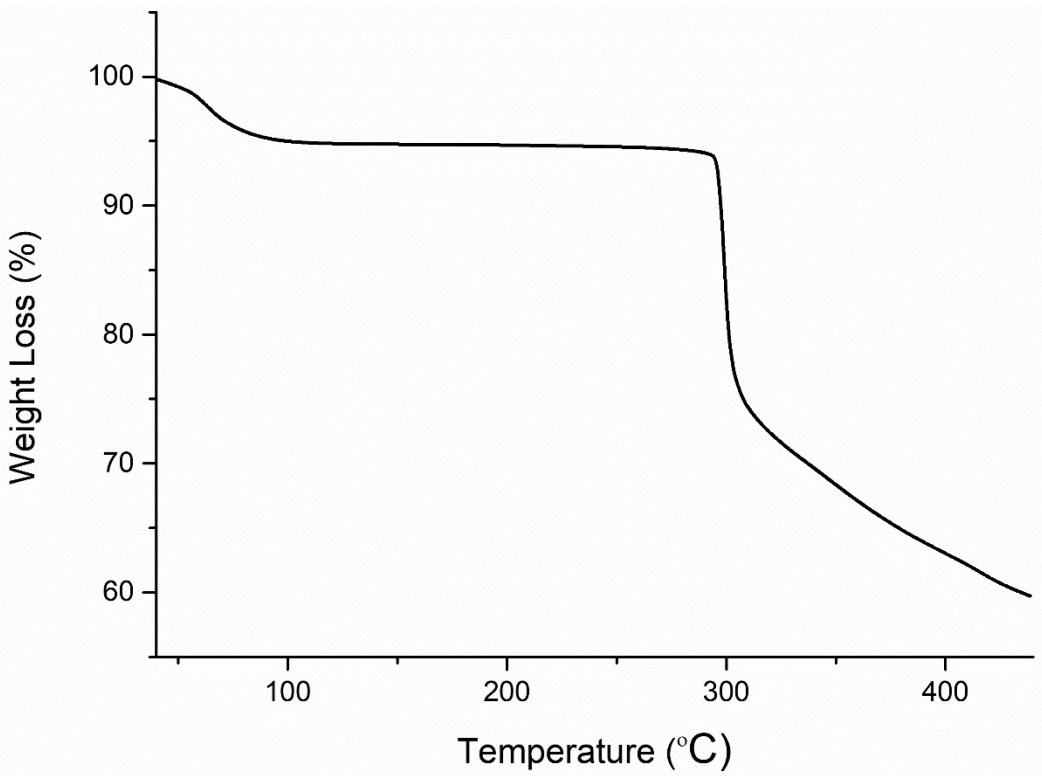

Figure S17. TGA trace of **1c.** A solvent weight loss of 5% is apparent between 30 – 110°C with decomposition occurring at ~295 °C.

5. Gas adsorption

Prior to activation, samples soaked in MeOH (x 7) over a period of 24 h, and activated under high vacuum at 90 °C for 4 h, followed by 65°C for 16 h.

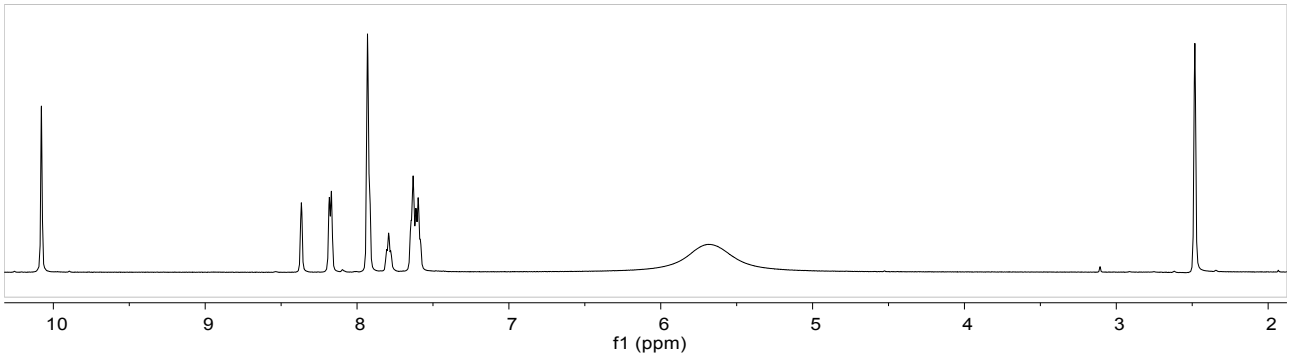

Figure S18. ^{1}H NMR spectrum (500 MHz/DMSO-d_6/DCl) showing an example of an acid digested sample (**1a**) post-activation.

Table S2: BET surface areas of **1a**-**c** as calculated from the 195 K CO_2 isotherms

Sample	**SA_{BET}** (m^2/g)
1a	178.67 ± 0.96
1b	108.67 ± 0.22
1c	32.73 ± 0.75

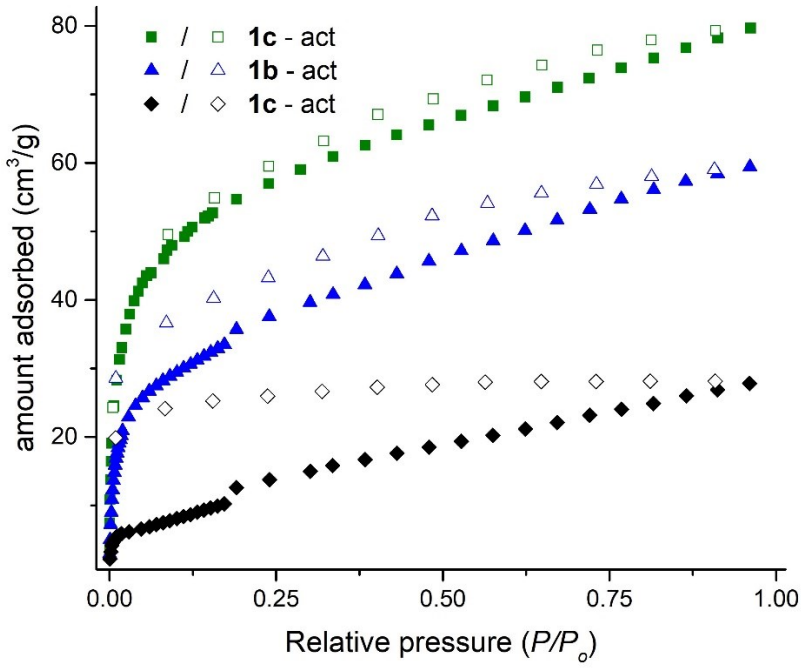

Figure S19. CO_2 isotherms of **1a-c** measured at 195 K. We note that **1b** and **1c** possess a small step at P/P_o ~ 0.2, which may relate to small structural changes involving pore opening upon adsorption.[5]

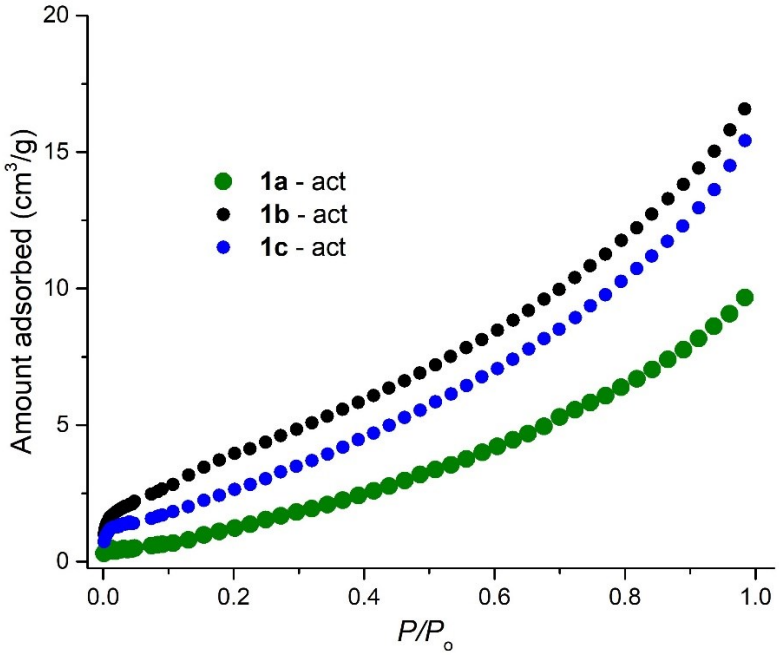

Figure S20. N_2 isotherms of **1a-c** measured at 77 K.

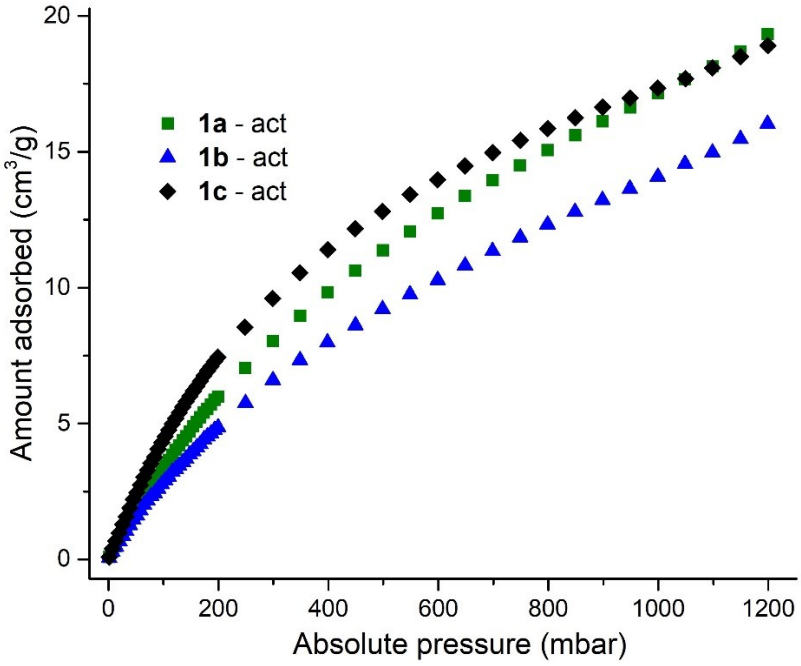

Figure S21. CO_2 uptake of **1a**-**c** at 293 K

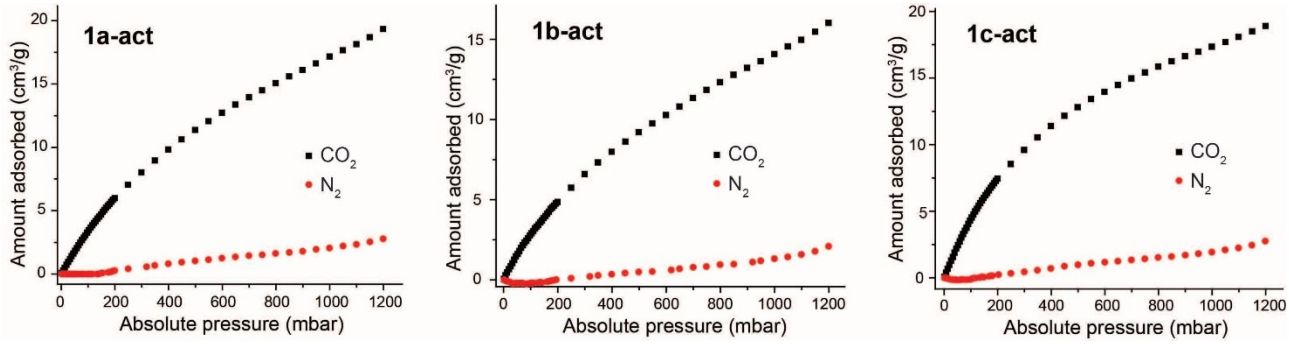

Figure S22. CO_2 and N_2 uptake of **1a-c** at 293 K

6. Calculations

Geometry optimisations of cage isomers were performed using PBE/def2-SVP (def2-TZVP for Cu) level of theory[6,7] in the gas phase starting from coordinates obtained from X-ray models (**1a**-**c**) or on models created on SPARTAN. To accelerate the DFT calculations, we employed the resolution-of-the-identity (RI) approximation with the corresponding auxiliary basis set (def2/J).[8] Note that for each structure, the axial coordinating solvents were omitted for the calculations. The optimised geometries are confirmed to be located at potential minima through frequency calculations. Single point energy calculations with PBE0/def2-TZVP level of theory[7,9] were performed on the optimised geometries. Dispersion corrections with damping function (D3BJ) were also employed.[10] All calculations were conducted using Orca 4.2.[11,12]

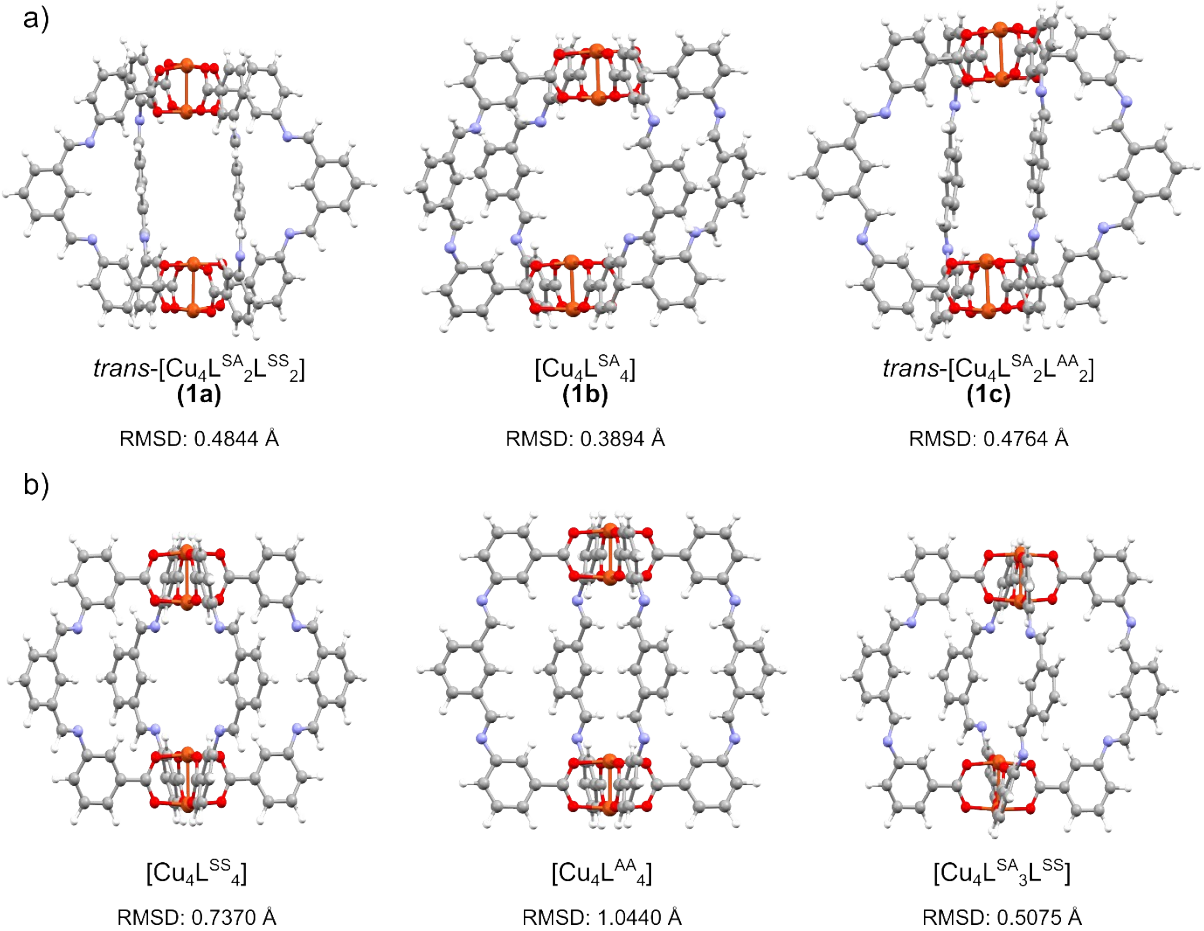

Figure S23. Geometry optimised structures (PBE/def2-SVP(def2-TZVP for Cu)) for a) experimental observed isomers **1a-c** and b) a selection of geometrically feasible but not experimentally observed isomers. Cu, O, N, C, and H atoms are represented by orange, red, blue, grey, and white spheres, respectively. Root mean square deviation values (RMSD) are calculated using atomic positions of all atoms except hydrogen.

Table S3: Relative energies (kJ/mol) of each isomer with respect to *trans*-[$Cu_4L^{SA}{}_2L^{AA}{}_2$] (**1c**) as calculated by different methods in the gas-phase.

Compound	**PBE/def2-SVP(TZVP)**	**PBE/def2-SVP(TZVP)-ZPVE**	**PBE0/def2-TZVP + D3BJ**
trans-[$Cu_4L^{SA}{}_2L^{SS}{}_2$] (**1c**)	0.0	0.0	0.0
[$Cu_4L^{SA}{}_4$] (**1b**)	1.323	0.415	3.272
[$Cu_4L^{SA}{}_3L^{AA}$]	10.502	9.465	12.263
trans-[$Cu_4L^{SA}{}_2L^{AA}{}_2$] (**1a**)	17.686	16.647	18.829
[$Cu_4L^{AA}{}_4$]	24.474	22.404	27.623
[$Cu_4L^{SS}{}_4$]	-4.439	-5.057	-1.731

In gas phase, the following trend of energetic stability is observed:

[$Cu_4L^{SS}{}_4$] > *trans*-[$Cu_4L^{SA}{}_2L^{SS}{}_2$] (**1c**) > [$Cu_4L^{SA}{}_4$] (**1b**) > [$Cu_4L^{SA}{}_3L^{AA}$]> *trans*-[$Cu_4L^{SA}{}_2L^{AA}{}_2$] (**1a**) > [$Cu_4L^{AA}{}_4$]

7. X-ray crystallography

7.1. General methods

Single crystals were mounted in paratone-N oil on a plastic loop. X-ray diffraction data for **1a** and **1c**, **1a**-**MeOH**, **1b**-**py** and **2** were collected at 100(2) K on the MX-1 or MX-2 beamline of the Australian Synchrotron.[13,14] X-ray diffraction data for **1b** was collected at 150(2) K on an Oxford X-Calibur single crystal diffractometer (λ = 0.7107 Å). Data sets were corrected for absorption using a multi-scan method, and structures were solved by direct methods using SHELXT[15] and refined with SHELXL[16] and ShelXle[17] as a graphical user interface. All non-hydrogen atoms were refined anisotropically and hydrogen atoms were included as invariants at geometrically estimated positions. The contribution of the electron density from disordered, pore-bound solvent molecules, which could not be modelled with discrete atomic positions were handled using the SQUEEZE[18] routine in PLATON,[19] which strongly improved all figures of merit (FOM). X-ray experimental data is given in Table S4 and S5.

Table S4: X-ray experimental data **1a**-**c**.

Compound	**1a**	**1b**	**1c**
CCDC number	2044789	2044787	2044788
Empirical formula	$C_{104}H_{92}Cu_4N_{12}O_{20}$	$C_{104}H_{92}Cu_4N_{12}O_{20}$	$C_{100}H_{84}Cu_4N_{12}O_{20}$
Formula weight	2084.05	2084.05	2027.95
Crystal system	Triclinic	Triclinic	Triclinic
Space group	*P*-1	*P*-1	*P*-1
a (Å)	14.027(3)	14.7652(8)	10.959(2)
b (Å)	14.475(3)	15.0291(8)	14.077(3)
c (Å)	15.468(3)	16.2398(7)	19.406(4)
α (º)	111.87(3)°	71.439(5)	106.27(3)
β (º)	101.96(3)°	73.953(4)	91.83(3)
γ (º)	92.36(3)°	71.422(5	101.78(3)
Volume (Å^3)	2826.9(12)	3176.3(3)	2800.7(11)
Z	1	1	1
Density (calc.) (Mg/m^3)	1.224	1.090	1.202
Absorption coefficient (mm^{-1})	0.809	0.720	0.814
F(000)	1076	1076	1044
Crystal size (mm^3)	0.21x0.1x0.08	0.24x0.23x0.11	0.22x0.18x0.10
θ range for data collection (º)	1.461 to 27.101	3.304 to 26.371	1.545 to 27.100
Reflections collected	36989	33354	36650
Observed reflections [R(int)]	10440 [0.0181]	12490 [0.0479]	10317 [0.0148]
Goodness-of-fit on F^2	1.027	0.977	1.039
R_1 [I>2σ(I)]	0.0436	0.0442	0.0340
wR_2 (all data)	0.1358	0.1039	0.0979
Largest diff. peak and hole (e.Å-3)	0.705 and -0.639	0.413 and -0.315	0.912 and -0.906
Data / restraints / parameters	10440 / 636 / 692	12490 / 444 / 638	10317 / 432 / 617

Table S5: X-ray experimental data for **1a-MeOH**, **1b-py** and **2**

Compound	**1a-MeOH**	**1b-Py**	**2**
CCDC number	2044791	2044792	2044790
Empirical formula	$C_{90}H_{62}Cu_4N_8O_{20}$	$C_{106}H_{84}Cu_4N_{12}O_{18}$	$C_{79}H_{63}Cu_2N_{11}O_8$
Formula weight	1829.63	2068.01	1421.48
Crystal system	Triclinic	Triclinic	Triclinic
Space group	*P*-1	*P*-1	*P*-1
a (Å)	13.937(3)	14.682(3)	10.994(2)
b (Å)	14.389(3)	15.055(3)	16.101(3)
c (Å)	15.592(3)	16.110(3)	21.413(4)
α (º)	111.23(3)	70.99(3)	96.75(3)
β (º)	102.10(3)	74.36(3)	99.90(3)
γ (º)	91.91(3)	71.24(3)	92.00(3)
Volume (Å^3)	2829.3(12)	3133.4(14)	3702.1(13)
Z	1	1	2
Density (calc.) (Mg/m^3)	1.074	1.096	1.275
Absorption coefficient (mm^{-1})	0.799	0.728	0.637
F(000)	934	1064	1472
Crystal size (mm^3)	0.12x0.1x0.07	0.08x0.05x0.04	0.21x0.1x0.08
θ range for data collection (º)	1.443 to 25.679	1.360 to 28.282	0.973 to 29.070
Reflections collected	34790	49244	25110
Observed reflections [R(int)]	9841 [0.0658]	14191 [0.0345]	13813 [0.0212]
Goodness-of-fit on F^2	1.054	1.025	1.039
R_1 [I>2σ(I)]	0.0603	0.0518	0.0440
wR_2 (all data)	0.1916	0.1614	0.1296
Largest diff. peak and hole (e.Å-3)	0.701 and -0.963	0.827 and -1.296	0.871 and -0.865
Data / restraints / parameters	9841 / 0 / 551	14191 / 466 / 634	13813 / 0 / 903

Table S6: SQUEEZE results for **1a-c, 1a-MeOH, 1b-py** and **2** as calculated by PLATON.

Isomer	**Squeeze void volume**	**Squeeze void count electrons**
1a	591	169 (3.5 DMA molecules)
1b	1052	322 (6.5 DMA molecules and 1 H_2O molecule)
1c	822	186 (4.65 DMF molecules)
1a-MeOH	1196	279 (15.5 MeOH molecules)
1b-py	1181	253 (3.5 DMA molecules and 2 pyridine molecules)
2	542	110 (2.75 DMF molecules)

7.2. Thermal ellipsoid plots

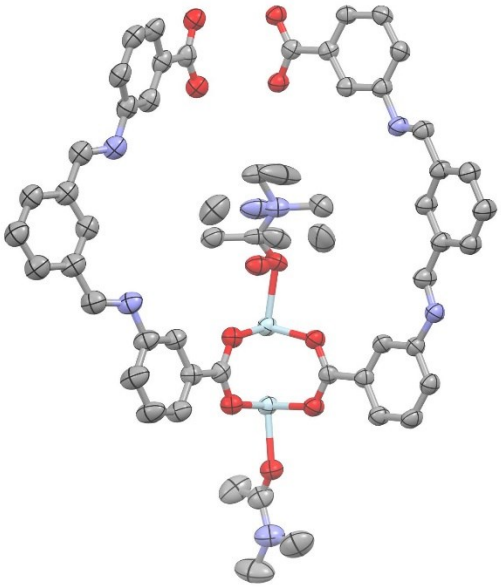

Figure S24. The asymmetric unit of the X-ray structures of **1a** with all non-hydrogen atoms shown as ellipsoids at the 50% probability level (hydrogen atoms omitted for clarity). C = grey, N = purple, O = red, Cu = light blue.

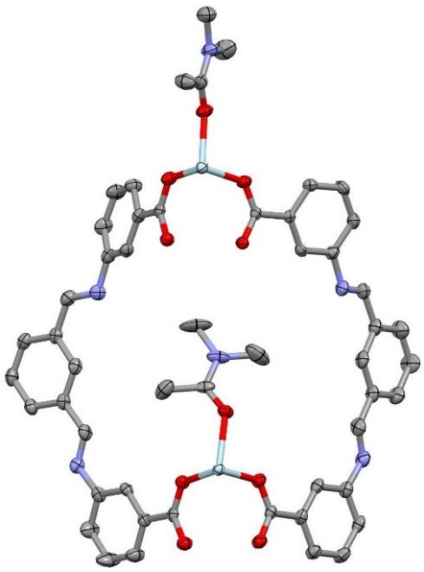

Figure S25. The asymmetric unit of the X-ray structures of **1b** with all non-hydrogen atoms shown as ellipsoids at the 50% probability level (hydrogen atoms omitted for clarity). C = grey, N = purple, O = red, Cu = light blue.

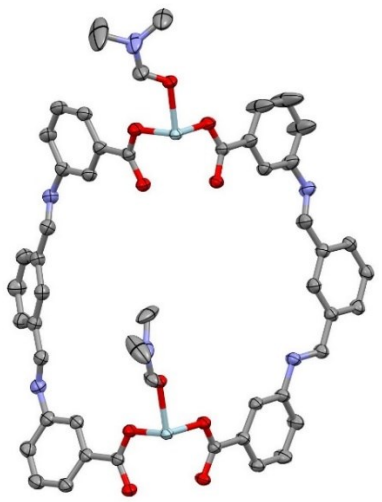

Figure S26. The asymmetric unit of the X-ray structures of **1c** with all non-hydrogen atoms shown as ellipsoids at the 50% probability level (hydrogen atoms omitted for clarity). C = grey, N = purple, O = red, Cu = light blue.

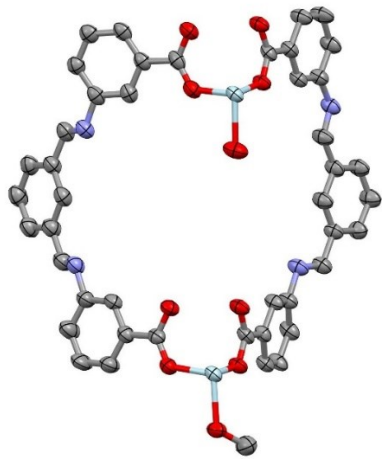

Figure S27. The asymmetric unit of the X-ray structures of **1a-MeOH** with all non-hydrogen atoms shown as ellipsoids at the 50% probability level (hydrogen atoms omitted for clarity). C = grey, N = purple, O = red, Cu = light blue.

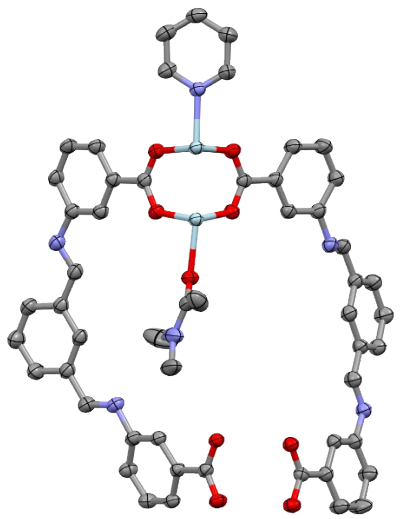

Figure S28. The asymmetric unit of the X-ray structures of **1b-py** with all non-hydrogen atoms shown as ellipsoids at the 50% probability level (hydrogen atoms omitted for clarity). C = grey, N = purple, O = red, Cu = light blue.

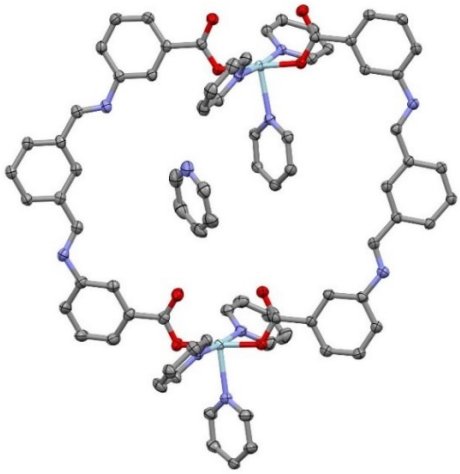

Figure S29. The asymmetric unit of the X-ray structures of **2** with all non-hydrogen atoms shown as ellipsoids at the 50% probability level (hydrogen atoms omitted for clarity). C = grey, N = purple, O = red, Cu = light blue.

8. A discussion on 1b and 1b-py

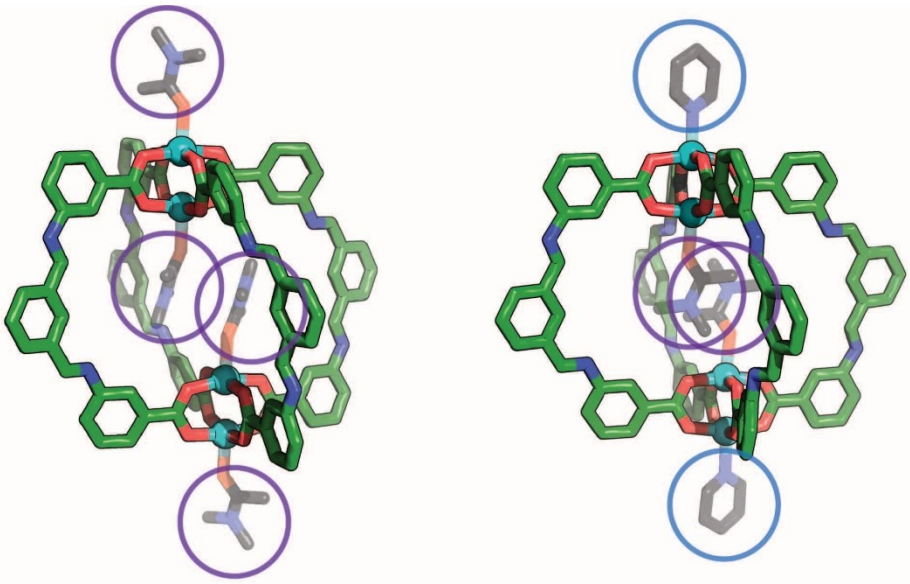

Name	**1b**	**1b-py**
Formula	$[Cu_4(L^{SA})_4(\mathbf{DMA})_2(\mathbf{DMA})_2]$	$[Cu_4(L^{SA})_4(\mathbf{py})_2(\mathbf{DMA})_2]$
Solvent medium	DMA, DiPE	DMA, pyridine*
[a]No. of possible solvatomorphs	1	4

Figure S30. A comparison of the solid-state structure and crystallisation conditions of **1b** and **1b**-**py**. Due to the presence of two types of coordinating solvents for **1b-py**, four solvatomoprhs are possible: **1b·DMA$_4$, 1b·DMA$_2$py$_2$**, **1b·py$_2$DMA$_2$** (observed), and **1b·py$_4$.** The selective crystallisation of a single solvatomorph suggests that **1b·py$_2$DMA$_2$** may be less soluble than that of **1b·DMA$_4$, 1b·DMA$_2$ py$_2$,** and **1b·py$_4$** in the DMA/pyridine solvent medium.*Structure obtained by the transformation of **2**. [a]Does not assume additional solvatomorphs from the coordination of H_2O.

The experiments carried out in this study suggests there are at least four interlinked factors which influence the solubility and preferential crystallisation of a particular cage isomer:

1) The ligand conformations within the cage assembly
2) The solubility of a particular cage isomer in a given solvent medium (e.g. **1a** and **1b** possess the same coordinating solvent (DMA) but are crystallised from different solvent media – DMA/MEOH vs. DMA/DiPE)
3) Solubilising effects from the solvent coordinating to the axial paddlewheel sites
4) Crystal packing effects; certain ligand configurations and coordinating solvents promote an efficient crystal packing of the cage molecules.

9. References

1 M. Kato, H. B. Jonassen and J. C. Fanning, *Chem. Rev.*, 1964, **64**, 99–128.

2 V. Brega, M. Zeller, Y. He, H. Peter Lu and J. K. Klosterman, *Chem. Commun.*, 2015, **51**, 5077–5080.

3 I. A. Riddell, M. M. J. Smulders, J. K. Clegg, Y. R. Hristova, B. Breiner, J. D. Thoburn and J. R. Nitschke, *Nat. Chem.*, 2012, **4**, 751–756.

4 W. M. Bloch, R. Babarao and M. L. Schneider, *Chem. Sci.*, 2020, **11**, 3664–3671.

5 G. A. Craig, P. Larpent, S. Kusaka, R. Matsuda, S. Kitagawa and S. Furukawa, *Chem. Sci.*, 2018, **9**, 6463–6469.

6 J. P. Perdew, K. Burke and M. Ernzerhof, *Phys. Rev. Lett.*, 1996, **77**, 3865–3868.

7 F. Weigend and R. Ahlrichs, *Phys. Chem. Chem. Phys.*, 2005, **7**, 3297–3305.

8 F. Weigend, *Phys. Chem. Chem. Phys.*, 2006, **8**, 1057–1065.

9 C. Adamo and V. Barone, *J. Chem. Phys.*, 1999, **110**, 6158–6170.

10 S. Grimme, S. Ehrlich and L. Goerigk, *J. Comput. Chem.*, 2011, **32**, 1456–1465.

11 F. Neese, *WIREs Comput. Mol. Sci.*, 2018, **8**, e1327.

12 F. Neese, F. Wennmohs, U. Becker and C. Riplinger, *J. Chem. Phys.*, 2020, **152**, 224108.

13 N. P. Cowieson, D. Aragao, M. Clift, D. J. Ericsson, C. Gee, S. J. Harrop, N. Mudie, S. Panjikar, J. R. Price, A. Riboldi-Tunnicliffe, R. Williamson and T. Caradoc-Davies, *J. Synchrotron Radiat.*, 2015, **22**, 187–190.

14 D. Aragao, J. Aishima, H. Cherukuvada, R. Clarken, M. Clift, N. P. Cowieson, D. J. Ericsson, C. L. Gee, S. Macedo, N. Mudie, S. Panjikar, J. R. Price, A. Riboldi-Tunnicliffe, R. Rostan, R. Williamson and T. T. Caradoc-Davies, *J. Synchrotron Radiat.*, 2018, **25**, 885–891.

15 G. M. Sheldrick, *Acta Crystallogr. Sect. A*, 2015, **71**, 3–8.

16 G. M. Sheldrick, *Acta Crystallogr. Sect. C*, 2015, **71**, 3–8.

17 C. B. Hubschle, G. M. Sheldrick and B. Dittrich, *J. Appl. Crystallogr.*, 2011, **44**, 1281–1284.

18 A. Spek, *Acta Crystallogr. Sect. C*, 2015, **71**, 9–18.

19 A. Spek, *Acta Crystallogr. Sect. D*, 2009, **65**, 148–155.